Dalton Transactions

ROYAL SOCIETY OF CHEMISTRY

PAPER

View Article Online
View Journal | View Issue

Cite this: *Dalton Trans.*, 2026, **55**, 3336

Unusual slow magnetic relaxation in a sulfate-bridged copper(II) complex with 1-(2-pyridylazo)-2-naphthol ligand

Meriem Goudjil, *[a,b] Carlo Andrea Mattei, [c] Leonardo Tacconi, [c] Laura Chelazzi[d] and Mauro Perfetti *[e]

We report an unprecedented one-pot route synthesis and in-depth characterizations of a new binuclear copper(II) complex with the tridentate PAN ligand (1-(2-pyridylazo)-2-naphthol). The compound of formula $[Cu_2(\mu\text{-}SO_4)(PAN)_2(H_2O)_2]$ was isolated as a highly crystalline material, where the two copper(II) centers are connected by a sulfate bridge. Single-crystal X-ray diffraction (SC-XRD) combined with UV-Vis spectroscopy confirms a square-pyramidal coordination around each Cu(II) center in both the solid state and solution. Remarkably, magnetic studies revealed an unconventional slow magnetic relaxation under applied dc fields, characterized by three field-dependent processes spanning more than four orders of magnitude in frequency. These findings broaden the design space of transition-metal molecular magnets by showing that simple sulfate bridging and π-conjugated ligands can engender complex relaxation dynamics in Cu(II) dimers.

Received 10th January 2026,
Accepted 25th January 2026

DOI: 10.1039/d6dt00068a

rsc.li/dalton

Introduction

Molecular compounds represent an essential class of materials providing experimental and theoretical models in fields such as bioinorganic chemistry,[1] catalysis,[2] and molecular magnetism.[3] Among these, copper(II) complexes have been central thanks to the $3d^9$ electronic configuration of the Cu(II) cation, which enables a rich diversity of coordination geometries (*e.g.* square planar, square pyramidal, distorted octahedral) and compelling magnetic properties.[4,5] Further, polynuclear copper(II) coordination complexes have been paradigmatic in advancing the understanding of magnetic exchange phenomena.[6–8] Several Cu(II) complexes have been explored as candidate molecular qubits due to their $S = 1/2$ electron spin and tunable electronic environments. A notable early example is the dithiolene system $(PPh_4)_4[Cu(mnt)_2]$, which exhibits exceptionally long spin coherence times at low temperature and observable coherence up to room temperature, demonstrating key qubit characteristics in a chemically tunable complex.[9] Theoretical studies on $[Cu(mnt)_2]^{2-}$ highlight how intramolecular vibrations influence decoherence and provide a framework for designing Cu-based qubits with improved resilience against spin–phonon coupling.[10] More recently, Cu(II) porphyrins have been investigated to understand the role of molecular structure and vibrational modes on spin relaxation dynamics, revealing that some distorted Cu porphyrins maintain significant coherence and offering a platform for tuning qubit performance through ligand environment.[11] Additionally, comprehensive reviews of Cu(II) systems frame these complexes within broader efforts to exploit their spin-relaxation properties for quantum information science.[12]

In the rational design of molecular magnetic materials, it is essential to consider not only the ligand field effects arising from the primary metal coordination sphere[13,14] but also the influence of weaker supramolecular interactions[15–18] (*e.g.* H-bonding, C–H–π and π–π interactions) that drive the solid-state crystal packing. Indeed, among the key factors that govern and modulate the magnetic phenomena are also those effects dictated by the phonon bath and through-space magnetic coupling (*i.e.* distance between magnetic spins and their relative orientation).[19] Furthermore, the deliberate incorporation of simple inorganic (*e.g.*, hydroxide, halide, sulfate) or extended organic bridging ligands (*e.g.*, oxalate, bipyridine) offers a powerful strategy to fine-tune magnetic interactions, enabling precise control over the enhancement or suppression of specific magnetic properties.[8]

[a]*Department of Industrial Engineering, University of Florence, via Santa Marta 3, Florence 50139, Italy. E-mail: meriem.goudjil@unifi.it*
[b]*Institute of Nanostructured Materials (ISMN)-National Research Council (CNR), Via P. Gobetti 101, Bologna, 40129 Italy*
[c]*Department of Chemistry "U. Schiff", University of Florence, Via della Lastruccia 3-13, Sesto Fiorentino, 50019 Firenze, Italy*
[d]*Centro di Cristallografia Strutturale, University of Florence, via della Lastruccia 3, Sesto Fiorentino, Florence 50019, Italy*
[e]*Department of Chemistry "U. Schiff", University of Florence and INSTM Research Unit, Via della Lastruccia 3-13, Sesto Fiorentino, 50019 Firenze, Italy. E-mail: mauro.perfetti@unifi.it*

The ligand 1-(2-pyridylazo)-2-naphthol (HPAN, generally referred to as PAN) is a versatile N-,N′-,O-donor chelating agent, widely recognized as one of the most effective spectrophotometric reagents for the detection and the extraction of a broad range of transition metals.[20,21] Its strong affinity for metal cations,[22–25] including Cu(II)[22,26–31] enables the formation of stable coordination complexes. Owing to its binding flexibility, the PAN ligand can adopt multiple binding modes behaving as a monodentate,[24] bidentate,[24,25] or as a tridentate[22,31] ligand, therefore facilitating diverse metal–ligand architectures. The conjugated π-network characteristic of PAN-based complexes has appeared attracting to promote electronic delocalization and π–π stacking potentially leading to magnetic coupling between adjacent Cu(II) centers.

To assess the structural diversity of PAN-containing coordination compounds, a comprehensive survey of the Cambridge Structural Database (CSD, version 6.00, April 2025) was conducted. The search retrieved 30 entries (see Tables S1 and S2), each featuring a PAN coordinated to either a transition metal such as Cu(II), Ru(II), Re(I), Re(III), Rh(III), Ir(III), Cr(III) and V(V) or rare-earth elements including Eu(III), Gd(III), Yb(III) and Tb(III). Of these, 28 structures possess complete crystallographic data, while two lack resolved 3D coordinates. Remarkably, only 8 of the identified complexes exhibit a dimeric configuration, highlighting the relative scarcity of PAN-based metal dimers within the current crystallographic landscape. Furthermore, these PAN dimers have received little attention in terms of detailed magnetic characterization, leaving their magnetic properties largely unexplored.

In light of this structural rarity and the intriguing magnetic potential of transition metal-bridged systems, we present herein the synthesis, single-crystal X-ray diffraction (SC-XRD) analysis, EPR spectroscopy, and SQUID magnetometry for a new dimeric Cu(II) complex with the tridentate Schiff-like ligand PAN and bridged by a single sulfate anion. Through a combined crystallographic analysis and modeling of the magnetic properties, we examine the structure–magnetism relationship, with particular emphasis on magnetic exchange pathways to reveal an unusual slow relaxation of magnetization behavior, which, to the best of our knowledge, is unprecedented among Cu(II) dimers containing solely $S = 1/2$ species.

Results and discussion

Synthetic procedure

The reaction between copper sulfate and one equivalent of the PAN ligand in a H_2O/EtOH solvent mixture proceeded smoothly without the need for a deprotonating agent (Scheme 1). The target copper complex was obtained as gold-brown needles with metallic luster, soluble in H_2O and most common organic solvents. The key structural feature driving the formation of a dimeric species is the bridging capability of the sulfate anion. Elemental analysis: (calc. %) C 71.97, H 4.83, N 16.79, and S 6.41; (found %): C 71.21, H 4.81, N 16.60, and S 6.56.

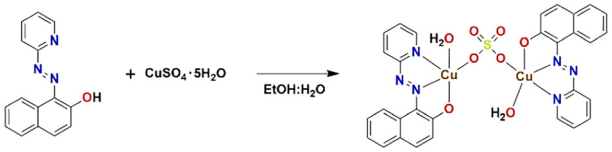

Scheme 1 Synthesis route of the μ-sulfato-bis(1-(2-pyridylazo)-2-naphtholato)-di-copper(II) complex.

FT-IR and UV-Vis spectral studies

The evidence for complex formation was first assessed through FT-IR and UV-Vis characterizations.

The IR spectra of the free PAN ligand and its Cu(II) dimer complex are shown in Fig. S1. The free ligand shows characteristic bands for phenolic ν(O–H) (broad, 3200–3600 cm^{-1}), aromatic ν(C–H) (2800–3200 cm^{-1}), see Fig. S1a, and strong azo ν(–N=N–) (1505 cm^{-1}) stretches.[32] The fingerprint region features overlapping ν(C=N)/ν(C=C) bands between 1535–1655 cm^{-1} and phenolic ν(C–O) at 1204 cm^{-1}.[33] Bands from 1115–1280 cm^{-1} correspond to –N=N–Ar deformation and ring breathing, with δ(C–H) out-of-plane bends at 840 and 750 cm^{-1}. Upon Cu(II) coordination, shifts in the azo (to 1509 cm^{-1}) and phenolic (to 1210 cm^{-1}) peaks indicate binding *via* azo nitrogen and phenolic oxygen.[34] A broad band at 3420 cm^{-1} confirms the presence of coordinated water (Fig. S1a). Bands at 1095 and 1052 cm^{-1} are assigned to ν(S=O) of the coordinated sulfate bridge (Fig. S1b).[35] Around 1000 cm^{-1}, the peak is assigned to both ν(S=O) and ν(Cu–O), while peaks from 645–600 cm^{-1} correspond to ν(Cu–N) and ν(Cu–O), confirming chelation.

The UV–Vis spectrum of free PAN is shown in Fig. S2a. The Gaussian deconvolution shows three principal absorptions: a $\pi \rightarrow \pi^*$ transition of the aromatic rings (~300 nm), an azo-centered $n \rightarrow \pi^*$ band with ILCT character (~420 nm), and a lower-energy $\pi \rightarrow \pi^*$ transition across the conjugated framework (~478 nm).[36] Upon coordination with Cu(II) in the sulfate-bridged dimer, the spectral profile evolves into five deconvoluted bands (see Fig. S2b). Intense high-energy features (230–360 nm) are still dominated by intra-ligand $\pi \rightarrow \pi^*$ and ILCT processes, followed by a band peaked at 420 nm attributed to azo $n \rightarrow \pi^*$ excitations. A broad feature spanning 450–700 nm, with a maximum at 558 nm, corresponds to phenolate → Cu(II) LMCT transitions and d–d contributions, consistent with previously reported bis-(μ_2-chloro)-bis(1-(2-pyridylazo)-2-naphtolto)-copper(II) (CCDC refcode: PAZNCO01).[28] The broadening likely results from dimerization effects perturbing the spin coupling across the sulfate bridge.[37]

Crystal structure of $[Cu_2(\mu\text{-}SO_4)(PAN)_2(H_2O)_2]$

The crystallographic analysis identified a new dimeric Cu(II) complex, namely $[Cu_2(\mu\text{-}SO_4)(PAN)_2(H_2O)_2]$, featuring mono-μ-sulfato bridging. The crystallographic data are reported in Table S3. The asymmetric unit shown in Fig. 1a includes two crystallographically independent Cu(II) sites, two independent PAN molecules, one sulfate anion, and two coordinated water

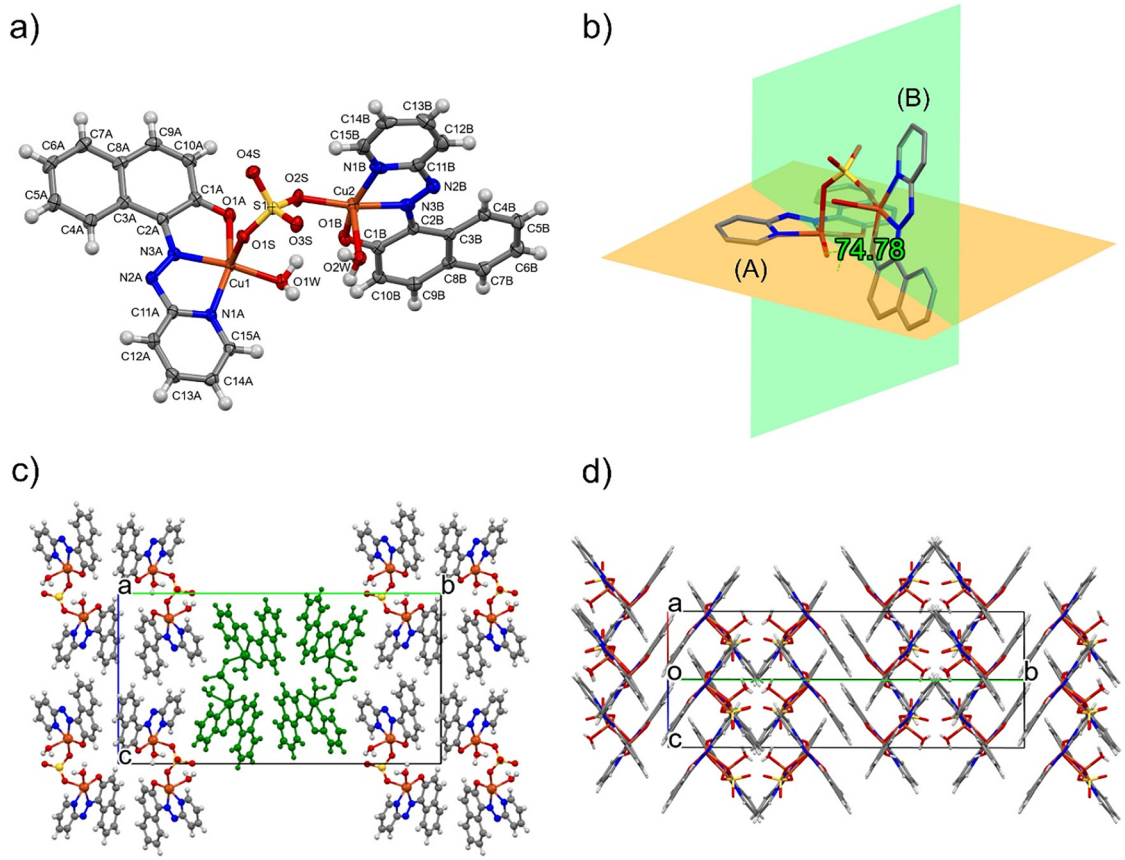

Fig. 1 Thermal ellipsoid plot at 50% probability level and labeling scheme for $[Cu_2(\mu\text{-}SO_4)(PAN)_2(H_2O)_2]$ (a); perspective view illustrating the dihedral angle between PAN ligand planes (b); crystal packing diagram (ball-and-sticks representation) viewed along [100] direction depicting highlighting centrosymmetric dimers in green (c); projection of the crystal structure (capped sticks representation) along [110] showing the herringbone packing motif (d). Color code: Cu, orange; C, grey; H, white; N, blue; O, red, and S, yellow.

molecules. Each Cu(II) ion links the PAN ligand in an N,N′,O tridentate mode, forming contiguous five-membered chelate rings. The coordination bond lengths are as follows: Cu–N(Py): 2.002(4)–2.010(3) Å, Cu–N(Azo): 1.949(3)–1.988(4) Å, and Cu–O (naphthol): 1.981(3)–1.987(3) Å.

The sulfate ligand, bridges the two $[Cu(PAN)]^+$ units in a bidentate μ_2-O,O′ mode (Harris notation: 2.1100 (ref. 38)) with an average S–O bond length of 1.477(3) Å and O–S–O angles ranging from 108(2)° to 111(2)°, consistent with tetrahedral (T_d) geometry.[39] It coordinates to Cu1 at the apical position (Cu1–O1S: 2.249(3) Å) and to Cu2 within the equatorial plane (Cu2–O2S: 1.946(3) Å), establishing a Cu1···Cu2 spacing of 4.717(1) Å. Each Cu(II) cation also binds to a water molecule: Cu1 in the equatorial plane (Cu1–O1W: 1.926(3) Å) and Cu2 in the apical position (Cu2–O2W: 2.302(3) Å). Both Cu(II) exhibit a $\{N_2O_3\}$ coordination environment, adopting a distorted square pyramidal geometry, supported by the trigonality index[40] (0.126 and 0.164 for Cu1 and Cu2, respectively). This geometry aligns with that observed in the related PAN-based Cu(II) monomeric (CCDC refcodes: KAKZOL and KAKZUR[29]) and dimeric (CCDC refcode: PAZNCO01[41]) complexes. Selected bond lengths (Å) and angles (°) for $[Cu_2(\mu\text{-}SO_4)(PAN)_2(H_2O)_2]$ are listed in Table S4. In this complex, the PAN ligands are oriented in a *trans* configuration relative to one another, with an angle of 74.78° between their intersecting planes (Fig. 1b).

The crystal structure of this complex reveals a compelling supramolecular organization, where individual molecules assemble into dimeric units (highlighted in green in Fig. 1c), related by an inversion center, as illustrated in the projection along the [100] crystallographic direction (Fig. 1c). Distinct and directional CH···π interactions stabilize these centrosymmetric dimers,[42] involving the naphthol moieties, specifically C7B–H7B···$\pi_{C3A-C8A}$: 2.892 Å/147° and C9B–H9B···$\pi_{C1A-C10A}$: 2.837 Å/132°; see Fig. 2a. Beyond the inversion-related dimers, additional structural cohesion arises from moderate O···H hydrogen bonding between dimeric units related by the *c*-glide plane (Fig. 2a and Table 1). Each molecule within the dimer engages in bifurcated hydrogen bonding with two symmetry-related neighbors *via* the sulfonate oxygen (O3S) and pyridine ring hydrogens, forming C13A–H13A···O3S (2.434(3) Å, 144(1)°) and C13B–H13B···O3S (2.376(3) Å, 146(1)°) contacts. These interactions culminate in the formation of an $R_2^2(18)$ ring motif that contributes to enhancing crystal stability.

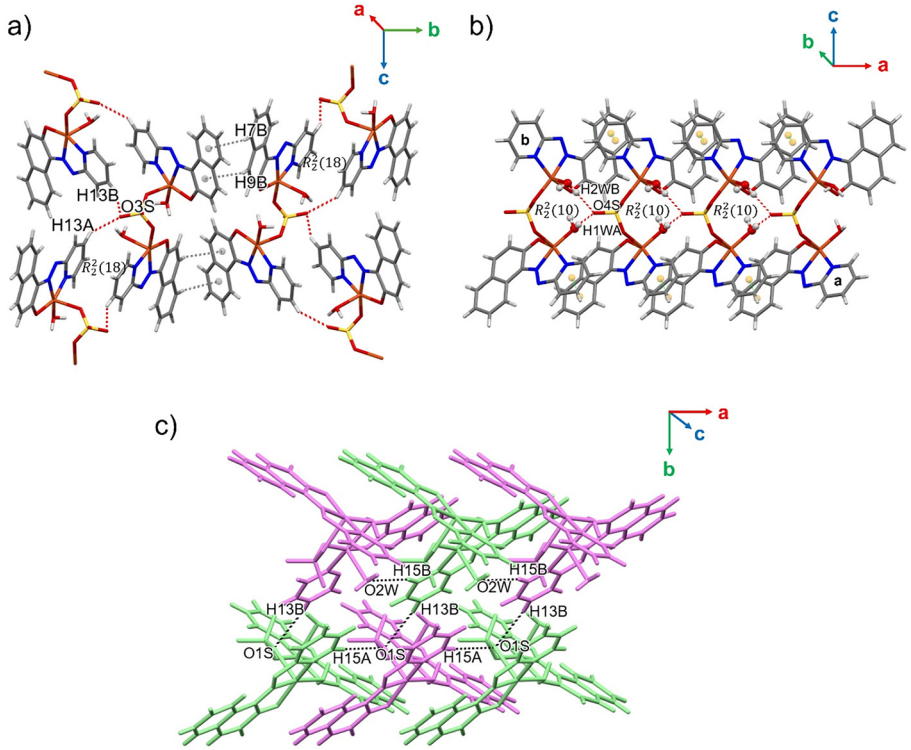

Fig. 2 Crystal packing views of $[Cu_2(\mu\text{-}SO_4)(PAN)_2(H_2O)_2]$ complex highlighting key non-covalent interactions: C–H···π and O···H contacts contributing to dimer stabilization (a); π–π stacking and O···H hydrogen bonding interactions reinforcing molecular alignment (b); extended O···H hydrogen bonding network forming a 3D supramolecular network (c).

Table 1 Hydrogen bond geometry parameters (Å, °) for $[Cu_2(\mu\text{-}SO_4)(PAN)_2(H_2O)_2]$

Type	D–H···A	D–A (Å)	H···A (Å)	D–H···A (°)	Symmetry operation
Intramolecular	C4A–H4A···N2A	2.938(5)	2.319(3)	122(1)	x, y, z
	C4B–H4B···N2B	2.928(5)	2.311(4)	122(1)	x, y, z
	O1W–H1WB···O1B	2.640(4)	1.842(3)	151(1)	x, y, z
	O2W–H2WA···O3S	2.731(4)	2.005(3)	139(1)	x, y, z
Intermolecular	O1W–H1WA···O4S	2.612(4)	1.788(3)	157(1)	$x + 1, +y, +z$
	O2W–H2WB···O4S	2.778(4)	1.907(3)	176(1)	$x + 1, +y, +z$
	C13A–H13A···O3S	3.255(5)	2.434(3)	144(1)	$x + 1/2, -y + 1/2, +z - 1/2$
	C13B–H13B···O3S	3.209(6)	2.376(3)	146(1)	$x - 1/2, -y + 1/2, +z + 1/2$
	C13B–H13B···O1S	3.341(6)	2.576(3)	137(1)	$x - 1/2, -y + 1/2, +z + 1/2$
	C15A–H15A···O1S	3.457(5)	2.565(3)	156(1)	$x + 1, +y, +z$
	C15B–H15B···O2W	3.233(5)	2.460(3)	138(1)	$x - 1, +y, +z$

The molecules align parallel to the (100) planes through π–π stacking interactions between pyridine (a/b) and phenyl rings (C3A–C8A/C3B–C8B), respectively, with centroid-to-centroid distances from 3.838 to 3.912 Å (Fig. 2b and Fig. S3).

These interactions not only consolidate the packing but also contribute to the electronic delocalization within the lattice. The sulfate anion plays a dual role: it bridges the Cu(II) centers and simultaneously engages in directional hydrogen bonding with coordinated water molecules, forming a periodic $R_2^2(10)$ motif (O1W–H1WA···O4S: 1.788(3) Å, 157(1)°; O2W–H2WB···O4S: 1.907(3) Å, 176(1)°; Fig. 2b). Additional weak O···H contacts along [100]: C15B–H15B···O2 W and C15A–H15A···O1S (Table 1 and Fig. 2c) and a further hydrogen bond along the *c*-axis (C13B–H13B···O1S) reinforces the 3D connectivity.

The arrangement of PAN ligands in *trans* configuration relative to each other, together with water molecules occupying distinct, apical and equatorial, positions foster a robust network of intramolecular hydrogen bonds. These include N–H···O and O–H···O interactions (Table 1), which stabilize the coordination sphere and strengthen the binuclear unit. Together with π–π stacking and C–H···π contacts, these interactions orchestrate a tightly knit lattice architecture.

Ultimately, the crystal structure manifests as chevron-like rows arranged in a herringbone pattern along the [110] direc-

tion (Fig. 1d). The combination of non-covalent interactions, including hydrogen bonding, π–π stacking, and C–H···π contacts, contributes meaningfully to the overall cohesion and structural integrity of the sulfate-bridged dimer.

Additional insight into the nature, strength, and relative contributions of the intermolecular contacts governing the crystal packing is provided by Hirshfeld surface analysis, as discussed in detail in the SI (Section 4).

The phase purity of the synthesized compound was confirmed by the perfect agreement between the experimental and simulated powder X-ray diffraction (P-XRD) patterns (see Fig. S4).

Magnetic studies

The compound was characterized with dc SQUID magnetometry. In Fig. 3, we report the χT *vs.* T curve recorded at H = 1 kOe (see Fig. S8 for the one recorded at H = 10 kOe). The room temperature value of the χT *vs.* T curve is 0.842 emu K mol^{-1}, in agreement with the Curie constant for two S = 1/2 spins (0.75 emu K mol^{-1}) with g factors slightly larger than two, as expected for 3d^9 Cu(II) ions. Below 50 K, the curve rapidly drops to *ca.* 0.69 emu K mol^{-1}. This jump can be attributed to a moderate antiferromagnetic coupling between the Cu(II) ions of the dimeric unit. In the inset of Fig. 3, we report the M *vs.* H curves recorded at 2, 5 and 10 K. The lowest-temperature magnetization reaches the value of 1.94μ_B at H = 5 T without full saturation. The reduced magnetization plots (Fig. S9) do not show any sign of significant magnetic anisotropy, corroborating the expected moderate coupling value.

The curves were fitted with a spin Hamiltonian containing a Zeeman and a Heisenberg coupling term. To avoid over-parametrization, the g factors of both ions were assumed to be isotropic and identical.

$$H = \sum_{i=1}^{2} \mu_B g \hat{S}_i \cdot \mathbf{B} + J\hat{S}_1 \cdot \hat{S}_2$$

The best simulation provided the following values: g = 2.12 and J = 0.83 cm^{-1}. Such simulation excellently reproduces both the χT *vs.* T and M *vs.* H curves (Fig. 3a and S8).

Continuous wave X-band EPR spectra of the compound (Fig. S10) recorded at three temperatures show a rather broad peak close to g = 2, which could be reproduced with our best simulation parameters.

Our model allows us to simulate the Zeeman diagram, as shown in Fig. 3 (z direction). In zero field, the singlet ground state and the triplet excited state are separated by the coupling constant 0.83 cm^{-1}, causing a level crossing at *ca.* 8.2 kOe.

The dynamic properties of the complex were investigated using ac magnetometry. At zero applied dc field, the compound does not show any sign of slow relaxation in the investigated frequency window. Upon applying a dc field at the lowest accessible temperature, multiple peaks in the out-of-phase magnetic susceptibility appear (Fig. 4a), revealing a complex relaxation behavior. In Fig. S11–S13 we report the best fits and associated parameters. At moderate fields (2–10 kOe), two distinct components are observed, separated by approximately four orders of magnitude in frequency. These are designated as LF (low frequency, around 0.5 Hz) and HF (high frequency, around 4000 Hz) processes.

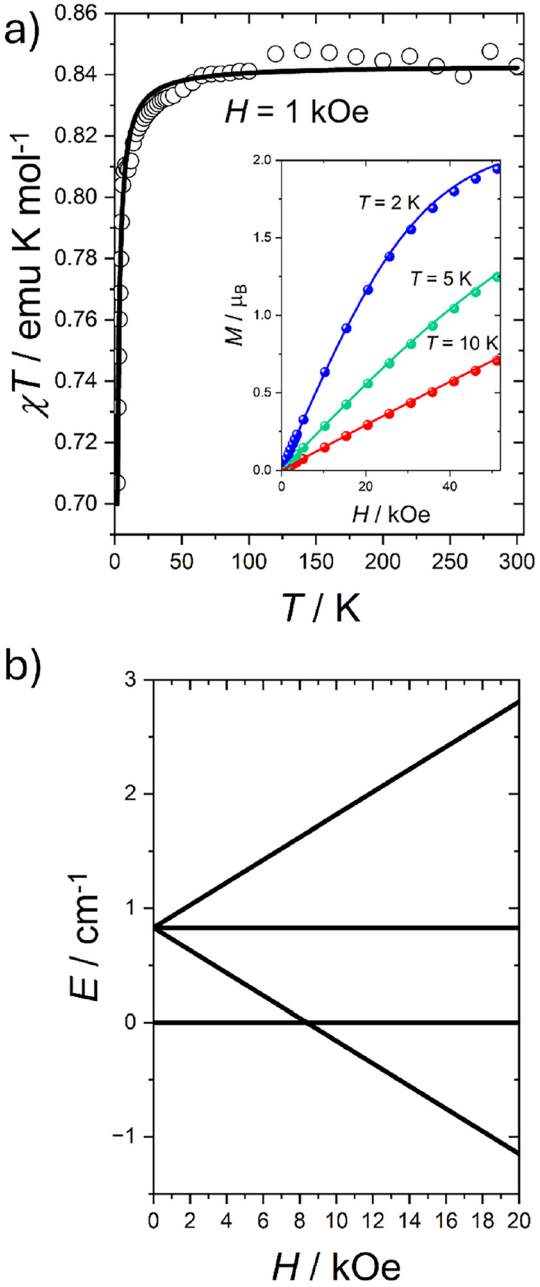

Fig. 3 Temperature dependence of the molar magnetic susceptibility plotted as χT *versus* T (a). Inset: field-dependent magnetization curves recorded at 2, 5, and 10 K. Dots are experimental points and solid lines are the best fit (see main text). Simulated Zeeman diagram along the z direction obtained from the best fit parameters, see text (b).

At higher fields, a third weaker peak appears as a shoulder at *ca.* 70 Hz, referred to as IF (intermediate frequency) process. At low dc fields, the HF process dominates the relaxation dynamics. As the field is increased, the LF contribution

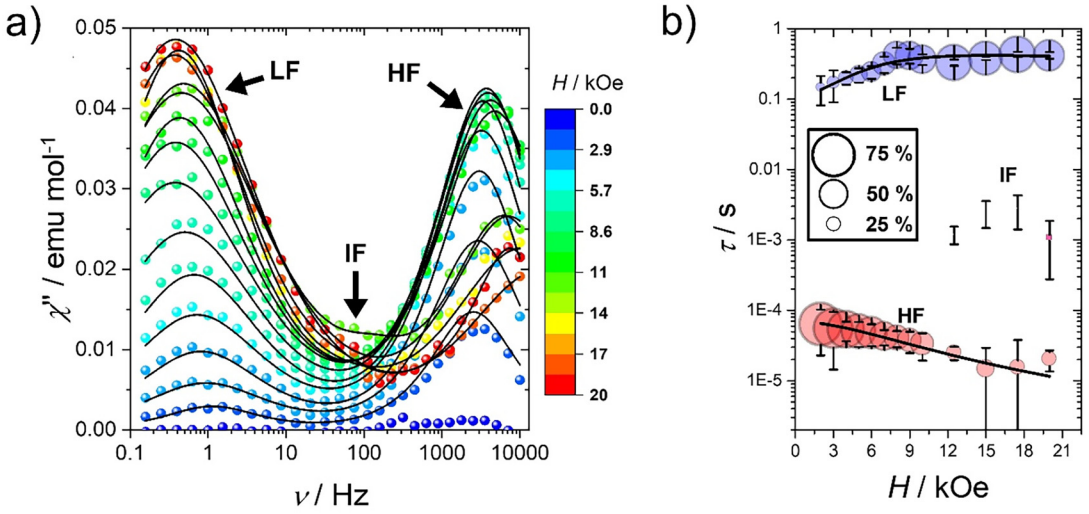

Fig. 4 Field evolution of the imaginary component of the magnetic susceptibility (a), and field evolution of the relaxation time, where the size of the symbols is proportional to the fraction of sample following a certain relaxation pathway (b) for $[Cu_2(\mu\text{-}SO_4)(PAN)_2(H_2O)_2]$. The error bars are extracted from the fit.

becomes progressively more significant, reaching an amplitude comparable to the HF process near 8 kOe. At higher fields, the LF process dominates, even when the IF process starts to be active.

The thermal evolutions of the LF and HF relaxation pathways were monitored at three different fields: 4, 8 and 15 kOe. At 4 kOe the HF process is dominant, and its thermal evolution was recorded (Fig. S14). The χ'' maximum shifts to higher frequencies with increasing temperature, indicating a thermally activated behavior. At 8 kOe, the two processes contribute almost equally. The LF process decays rapidly with the temperature (Fig. S15) suggesting the dominance of QT. On the contrary, the HF process is still markedly temperature-dependent (Fig. S16). At 15 kOe, the most favorable relaxation channel is LF. The χ'' peak decreases in intensity with increasing temperature without a significant change in its position (Fig. S17), indicating a near temperature-independent relaxation. The large distribution values ($\alpha > 0.44$) that we obtain from the fit (see after) corroborate our assignment. This complex relaxation behavior is quite peculiar and, to the best of our knowledge, unreported for dimers containing only $S = 1/2$ species. However, there are several examples in literature of similar dynamics in mononuclear,[43–49] dimeric,[47,50–53] trimeric,[52–57] and tetrameric[52,53,58,59] complexes.

To rationalize the experimental behavior, the ac susceptibility data were fitted using a Debye model considering two (low field) or three (high fields) components to extract the most probable relaxation time (τ), its distribution (α) and the difference between the isothermal and adiabatic susceptibility ($\chi_T - \chi_S$). In Fig. 4b, we report the evolution of the relaxation times of the two relaxation pathways with an applied dc magnetic field at $T = 2$ K. The dimension of the symbols in the figure is proportional to the fraction of spins following that specific relaxation pathway and was obtained by dividing $\chi_T - \chi_S$ for a certain process by the sum of all $\chi_T - \chi_S$ active at that field.[60] Plots of the single $\chi_T - \chi_S$ and α values are reported in SI (Fig. S12 and S13). In Fig. 5, we report the temperature dependences of the relaxation times extracted for the HF process at both 4 and 8 kOe. To assess information regarding the microscopic origin of the LF and HF processes we fitted the experimental relaxation times with appropriate models. The IF process was not fitted due to its scattered behavior and minor contribution to the relaxation (see symbol size in Fig. 4).

The field-induced LF relaxation process has been observed across a wide variety of systems, from quasi-isotropic[5,48,61] to anisotropic[43,51,54] metal centers, in both mononuclear and polynuclear complexes. Its low-temperature, field-dependent behavior has constant features: at low applied fields, the χ'' signal grows in intensity, and the relaxation time increases, reflecting the progressive suppression of quantum tunneling of magnetization (QTM). At higher fields, the relaxation time typically shortens, indicating the onset of a direct process. In contrast, temperature-dependent measurements at a fixed field usually reveal only a weak variation of the relaxation time, or a rapid disappearance of the χ'' peak upon heating, in agreement with our observations. Magnetic dilution experiments[43,50,54] consistently lead to the complete suppression of this relaxation channel, while modifications of the thermal contact between the sample and the cryogenic bath alter its characteristic time,[58] either accelerating or slowing it down. Together, these findings unambiguously indicate that the LF process originates from collective effects, involving spin–spin relaxation and/or spin–phonon bottleneck phenomena rather than from intrinsic single-ion dynamics.

Our observations of the LF process are consistent with the literature. Since no clear temperature dependence could be extracted for the LF process of our sample, insight into its origin can only be gathered from its field dependence. Qualitatively, the relaxation follows a trend consistent with previous reports. At low fields, the relaxation progressively slows

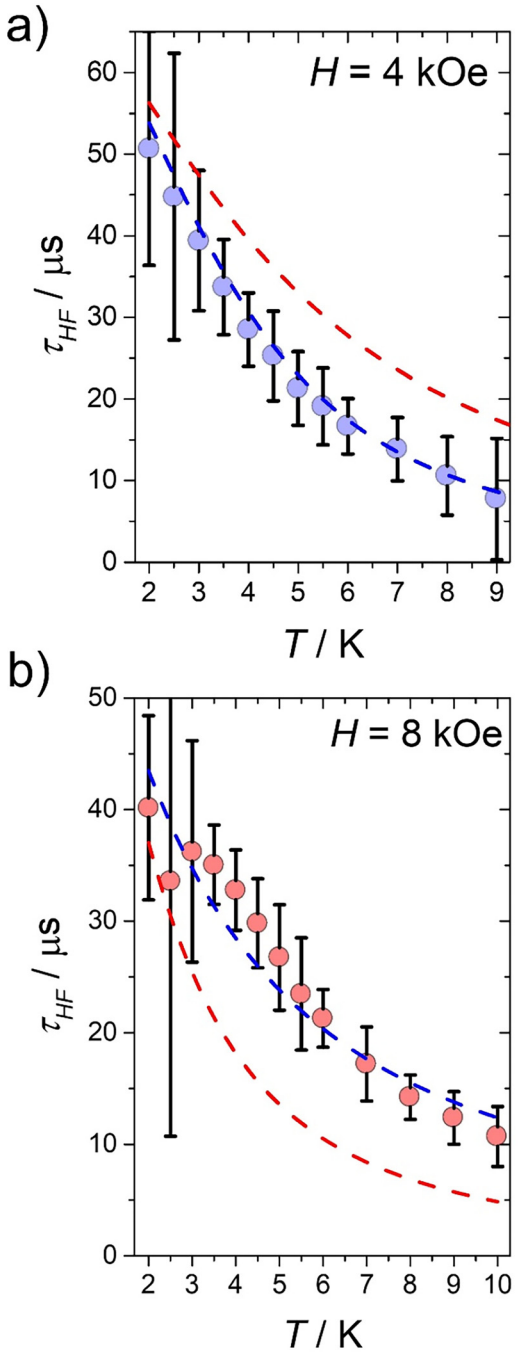

Fig. 5 Magnetic relaxation time *versus* temperature: at 4 kOe (a) and 8 kOe (b), where the HF process is thermally activated. Red dashed lines indicate the simulations performed with a shared temperature exponent n = 1.69, while blue dashed lines indicate the simulations performed with n = 2.12 at 4 kOe and n = 1.27 at 8 kOe, as described in main text.

down up to 8.5 kOe, reflecting a suppression of the QTM. Upon further increasing the field, the process accelerates, reaching a minimum relaxation time around 12.5 kOe, and subsequently slows again at higher fields. This non-monotonic behavior suggests the coexistence and gradual balance between field-induced suppression of tunneling and the onset of a direct mechanism. Therefore, we have attempted a fit using a combination of the two processes:

$$\tau_{\mathrm{LF}}{}^{-1} = \frac{B_1}{1 + B_2 H^2} + D \cdot T \cdot H^m$$

The best fit delivered the following parameters: B_1 = 8(2) s^{-1}, B_2 = 7(6) 10^{-8} Oe^{-2}, D = 1.5(7.0) 10^{-2} s^{-1} Oe^{-m} K^{-1}, m = 0.4 (5). Our fit (straight lines in Fig. 4b) replicates well the overall trend but fails to reproduce the fine structure, consistent with the relatively large uncertainties in the best-fit parameters.[45,62]

By contrast, the HF relaxation process is intrinsic and system-dependent, reflecting the specific dynamics of each compound. It can appear even in the absence of an external magnetic field,[56,58] if quantum tunneling is sufficiently quenched by local anisotropy. In strongly anisotropic systems, its behavior has been described by a two-phonon Orbach mechanism involving excitation to the first crystal field level,[51,56] or by a combination of Orbach and Raman pathways at higher temperatures.[62] In quasi-isotropic systems, where the crystal field splitting is small, the HF relaxation has instead been attributed to a phonon-bottleneck process,[46,48,51,55] which effectively mimics a low exponent Raman law ($n \approx 2$). The field dependence of this process is generally weak and monotonic, and its persistence upon magnetic dilution confirms its single-ion nature.

The HF relaxation process can be analyzed through its temperature and field dependencies, both of which provide information on the underlying mechanism. Since increasing either the magnetic field or the temperature accelerates the relaxation, the data were modelled using a function that accounts for both effects, shown in the following equation:

$$\tau_{\mathrm{HF}}{}^{-1} = \Gamma + D \cdot T^n \cdot H^m$$

The first term indicates a field-independent QTM contribution, while the second term corresponds to a Raman-modified direct process. As a matter of fact, in a fixed magnetic field it resembles a Raman relaxation ($\tau_{\mathrm{Raman}}{}^{-1} \propto T^n$) while in a fixed temperature it follows a direct dependence ($\tau_{\mathrm{Direct}}{}^{-1} \propto H^m$). A simultaneous fit of the three datasets yielded the following best-fit parameters: Γ = 14 384(219) s^{-1}, D = 1.5(2) 10^{-4} s^{-1} Oe^{-m} K^{-n}, m = 1.89(19), n = 1.69(51). The corresponding fits are shown in Fig. 4b (black lines) and 5 (dashed red lines). While the agreement with the experimental field dependence is satisfactory, noticeable deviations appear in the temperature dependencies: the relaxation rate is overestimated at 4 kOe and underestimated at 8 kOe. This behavior indicates that the temperature exponent n, and thus the effective spin–phonon coupling, varies with field strength. To test this, the datasets at 4 kOe and 8 kOe were refitted individually using the same model, fixing Γ, D and m to the values obtained above and allowing n to vary freely. The resulting exponents are n = 1.27 (8) at 4 kOe and n = 2.12(11) at 8 kOe. The new simulations (dashed blue lines in Fig. 5) reproduce the experimental data accurately, demonstrating the field dependence of the effective thermal exponent. Additionally, the Raman exponent near 2 supports the interpretation of a phonon-bottleneck[63,64] modi-

fied direct process as the origin of the observed experimental behavior. The requirement of a field-dependent temperature exponent has also been reported for a quasi-isotropic Mn(II) complex[46] and is clearly visible also in the experimental data of a one-dimensional Co(II) chain.[43] As for the LF process, magnetic dilution could unravel the origin of this process. However, our attempts to synthesize the same compound with Zn^{2+} did not lead to any isostructural complex.

Conclusions

The sulfate-bridged Cu(II) dimer $[Cu_2(\mu\text{-}SO_4)(PAN)_2(H_2O)_2]$ exemplifies how simple inorganic linkers and π-conjugated ligands can produce unexpectedly rich magnetic behavior. Structurally, the complex features a distorted square-pyramidal $\{N_2O_3\}$ environment at each Cu center, with the sulfate ion bridging equatorially to one Cu(II) and apically to the other, generating non-equivalent ligand fields that impart slight axial character to the Cu(II) ions. The dimeric molecules engage in symmetrical interactions *via* an extensive network of O···H hydrogen bonds and π–π stacking contacts, resulting in a robust 3D supramolecular architecture. Magnetically, the dimer exhibits an antiferromagnetic Heisenberg coupling of 0.83 cm^{-1}. Dynamics measurements displayed a peculiar field-dependent relaxation consisting of two main processes, one occurring at low frequency and one at high frequency. The former is dominated by a field-dependent QTM and direct mechanisms, while the latter is governed by a phonon-bottleneck modified direct process. This rich magnetic relaxation is, to the best of our knowledge, reported here for the first time for $S = 1/2$ dimer. The high-frequency channel shows an unexpected temperature dependence at the investigated fields. These findings broaden the design space for transition-metal molecular magnets and prompt questions regarding the role of sulfate bridges and π-conjugated ligands in fine-tuning the relaxation behavior. Future work will focus on tuning ligand environments to target compounds that could be magnetically diluted, and exploring heterometallic analogues to clarify the origin of these field-dependent processes and assess their potential in quantum information and low-temperature magnetic devices.

Experimental section

Materials and methods

The reagents used were copper sulfate pentahydrate ($CuSO_4{\cdot}5H_2O$, ≥98.0%), 1-(2-pyridylazo)-2-naphthol "PAN" ($C_{15}H_{11}N_3O$, indicator grade), and ethanol (EtOH, spectroscopic grade), all purchased from Sigma-Aldrich and used as received without further purification.

Elemental analysis

Elemental analysis was carried out using a EuroVector EA3100 elemental analyzer (CHNS).

FT-IR and UV-Vis methods

Spectral measurements were carried out for the PAN ligand and the synthesized copper complex. Fourier-transform infrared (FTIR) spectra were recorded in KBr pellet employing a Bruker Vertex 70 FT-IR spectrometer equipped with a CO_2 and H_2O purging system. UV-Vis absorption spectra were measured in EtOH (10^{-6} M) using a Jasco-550 UV–Vis spectrophotometer.

Single-crystal X-ray diffraction (SC-XRD)

A thin needle measuring 0.14 × 0.02 × 0.02 mm was mounted on a Cryoloop and transferred to the goniometer head for flash cooling at 150 K. X-ray diffraction data were collected using a Bruker D8 Venture (Bruker AXS) diffractometer equipped with an IμS 3.0 Incoatec micro-focus source, generating a monochromatic Cu K_α radiation (λ = 1.54178 Å) and a Photon II CPAD detector. A hemisphere of data was acquired up to a maximum 2θ of 137°. Data processing, including integration, absorption correction, and scaling, was carried out using the SAINT and SADABS software.[65] Details of the structure solution and refinement are available in the SI.

Powder X-ray diffraction (P-XRD)

P-XRD data were collected on a Bruker D8 diffractometer equipped with a sealed-tube copper X-ray source (λ $K_{\alpha1}$ = 1.5406 Å) and Bruker LYNXEYE-XE detector. The powder sample was packed into a 0.5 mm diameter glass capillary, and data were acquired over a 2θ range from 5 to 90°, with a step size of 0.01° and a scanning rate of 6 s per step.

X-band electron paramagnetic resonance (EPR)

EPR measurements were performed on a ground powder using an X-band ($\nu \approx$ 9.4 GHz) Elexsys E500 instrument (Bruker) equipped with a microwave frequency counter. An Oxford Instruments ESR900 continuous He flow cryostat was used to achieve low temperatures. An ER4122SHQE EPR resonator (Bruker) was used for the measurements.

Magnetic characterization

A Quantum Design Magnetic Properties Measurement System (MPMS) magnetometer equipped with a Superconducting Quantum Interference Device (SQUID) was used to perform both dc and ac magnetic characterization. The high-frequency ac measurements (100–10 000 Hz) were conducted in a Quantum Design PPMS equipped with ac susceptometry coils. Temperature- and field-dependent dc magnetization measurements were conducted on the Cu(II) complex sample (32.19 mg) within the temperature range of 2.0–300 K and at several fields ranging from 0 to 5 T. The sample was wrapped in Teflon and pressed into a pellet. The molar paramagnetic susceptibility of the complex was determined by considering the intrinsic diamagnetic contribution of the compound estimated using Pascal's constants.[66] Experimental results were modeled using a home-made MATLAB script based on the EasySpin package.[67] The ac susceptibility measurements were

carried out over a frequency range from 0.16 to 10 000 Hz in a field (0–20 kOe) and temperature (2.0–10 K) range. The ac susceptibility data were fitted using an in-house developed program.[68]

Synthesis

$CuSO_4 \cdot 5H_2O$ (0.5 mmol; 124.8 mg) was dissolved in a mixture of 10 mL of EtOH and 5 mL of deionized H_2O and subsequently stirred at room temperature for 15 minutes. This solution was then added dropwise to a separately prepared solution of the PAN ligand (0.5 mmol; 124.6 mg) dissolved in 10 mL of EtOH, maintained at 38 °C under continuous stirring. Upon addition of the copper salt, the reaction mixture immediately developed a deep red-wine coloration. Stirring continued for an additional 15 minutes. The resulting solution was then filtered and allowed to evaporate slowly at ambient conditions. Over the course of two days, thin brown needle-like crystals formed as the solvent gradually evaporated. The isolated crystalline product was obtained in a yield of ~74%. The synthetic route is illustrated in Scheme 1.

Author contributions

MG synthesized the complex and performed chemical characterization, assisted by CAM. LC cured the structural resolution. MP, CAM and LT performed the magnetic measurements (dc, ac, EPR) and modelling. All authors contributed in the manuscript writing.

Conflicts of interest

There are no conflicts to declare.

Data availability

The data supporting this article are included in the supplementary information (SI). Supplementary information: CCDC survey, IR and UV-Vis data, structure determination details, additional structural diagrams, Hirshfeld surface analysis (methodology and discussion), and magnetic measurements. See DOI: https://doi.org/10.1039/d6dt00068a.

CCDC 2264081 contains the supplementary crystallographic data for this paper.[69]

Acknowledgements

The authors gratefully acknowledge the use of X-ray diffraction facilities at the Centro di Cristallografia Strutturale (CRIST), University of Florence. M. G. thanks Dr. Eugenio Lunedei (Institute for the Study of Nanostructured Materials, Italian Research Council, ISM-CNR, Bologna) for providing access to infrared and UV–Vis characterization facilities.

References

1 F. K. Jørgensen, M. G. Delcey and E. D. Hedegård, *Phys. Chem. Chem. Phys.*, 2024, **26**, 17443–17455.
2 E. Roduner, *Chem. Soc. Rev.*, 2014, **43**, 8226–8239.
3 A. Raza and M. Perfetti, *Coord. Chem. Rev.*, 2023, **490**, 215213.
4 R. L. Carlin, *Magnetochemistry*, Springer, 1986, pp. 1–18.
5 R. Boča, C. Rajnák, J. Titiš and D. Valigura, *Inorg. Chem.*, 2017, **56**, 1478–1482.
6 A. Ozarowski, *Inorg. Chem.*, 2008, **47**, 9760–9762.
7 R. Maurice, K. Sivalingam, D. Ganyushin, N. Guihery, C. De Graaf and F. Neese, *Inorg. Chem.*, 2011, **50**, 6229–6236.
8 I. Castro, M. L. Calatayud, C. Yuste, M. Castellano, R. Ruiz-Garcia, J. Cano, J. Faus, M. Verdaguer and F. Lloret, *Polyhedron*, 2019, **169**, 66–77.
9 K. Bader, D. Dengler, S. Lenz, B. Endeward, S.-D. Jiang, P. Neugebauer and J. Van Slageren, *Nat. Commun.*, 2014, **5**, 5304.
10 L. Escalera-Moreno, N. Suaud, A. Gaita-Arino and E. Coronado, *J. Phys. Chem. Lett.*, 2017, **8**, 1695–1700.
11 N. P. Kazmierczak, N. E. Lopez, K. M. Luedecke and R. G. Hadt, *Chem. Sci.*, 2024, **15**, 2380–2390.
12 M. Wakizaka and M. Yamashita, *Chem. Phys. Rev.*, 2025, **6**(1), 01130.
13 P. C. Bunting, M. Atanasov, E. Damgaard-Møller, M. Perfetti, I. Crassee, M. Orlita, J. Overgaard, J. van Slageren, F. Neese and J. R. Long, *Science*, 2018, **362**, eaat7319.
14 A. S. Manvell, R. Pfleger, N. A. Bonde, M. Briganti, C. A. Mattei, T. B. Nannestad, H. Weihe, A. K. Powell, J. Ollivier and J. Bendix, *Chem. Sci.*, 2024, **15**, 113–123.
15 C. A. Mattei, B. Lefeuvre, V. Dorcet, G. Argouarch, O. Cador, C. Lalli and F. Pointillart, *Magnetochemistry*, 2021, **7**, 150.
16 A. A. Pavlov, Y. V. Nelyubina, S. V. Kats, L. V. Penkova, N. N. Efimov, A. O. Dmitrienko, A. V. Vologzhanina, A. S. Belov, Y. Z. Voloshin and V. V. Novikov, *J. Phys. Chem. Lett.*, 2016, **7**, 4111–4116.
17 G. Wang, Z. Jin, Y. Chen, F. Chen and Q. Chen, *J. Mol. Struct.*, 2025, **1336**, 142047.
18 S. S. Leiszner, M. Perfetti, E. Damgaard-Møller, Y.-S. Chen and B. B. Iversen, *Dalton Trans.*, 2024, **53**, 19246–19255.
19 S. Mondal, J. Netz, D. Hunger, S. Suhr, B. Sarkar, J. van Slageren, A. Köhn and A. Lunghi, *ACS Cent. Sci.*, 2025, **11**, 550–559.
20 I. Narin and M. Soylak, *Talanta*, 2003, **60**, 215–221.
21 K. Sarker and R. Ullaha, *Int. J. Chem. Stud*, 2013, **1**, 2321–4902.
22 R. A. Taylor, A. J. Lough, T. Seda, P. K. Poddutoori and M. T. Lemaire, *Polyhedron*, 2017, **123**, 462–469.
23 Y. Wu, J. Wang, X. Kong, C. Sheng, R. Wang, N. Peyghambarian, R. A. Norwood and Z. Zheng, *Inorg. Chim. Acta*, 2011, **370**, 346–352.
24 P. Mondal, A. Hens, S. Basak and K. K. Rajak, *Dalton Trans.*, 2013, **42**, 1536–1549.

25 S. Dinda, D. Jana, R. M. Gomila, A. Frontera, S. Roy, S. C. Patra, K. Pramanik and S. Ganguly, *Cryst. Growth Des.*, 2024, **24**, 3342–3354.
26 H. Adams, R. M. Bucknall, D. E. Fenton, M. Garcia and J. Oakes, *Polyhedron*, 1998, **17**, 4169–4177.
27 S. Ooi, D. Carter and Q. Fernando, *Chem. Commun.*, 1967, 1301–1302.
28 G. R. Desiraju, H. R. Luss and D. L. Smith, *J. Am. Chem. Soc.*, 1978, **100**, 6375–6382.
29 H. Wada, M. Shiro, A. Yuchi and G. Nakagawa, *Bull. Chem. Soc. Jpn.*, 1988, **61**, 3869–3875.
30 W.-B. Yu, Q.-Y. He, X.-F. Ma, H.-T. Shi and X. Wei, *Dalton Trans.*, 2015, **44**, 351–358.
31 C. Wang, J. Niu, J. Li and X. Ma, *Inorg. Chim. Acta*, 2017, **464**, 81–87.
32 G. Socrates, *Infrared and Raman characteristic group frequencies: tables and charts*, John Wiley & Sons, 2004.
33 K. Nakamoto, *Infrared and Raman spectra of inorganic and coordination compounds, part B: applications in coordination, organometallic, and bioinorganic chemistry*, John Wiley & Sons, 2009.
34 K. Pramanik and B. Adhikari, *Polyhedron*, 2010, **29**, 1015–1022.
35 K. W. Paul, M. J. Borda, J. D. Kubicki and D. L. Sparks, *Langmuir*, 2005, **21**, 11071–11078.
36 M. Montalti, A. Credi, L. Prodi and M. T. Gandolfi, *Handbook of photochemistry*, CRC press, 2006.
37 J. Mroziński and E. Heyduk, *J. Coord. Chem.*, 1984, **13**, 291–298.
38 R. A. Coxall, S. G. Harris, D. K. Henderson, S. Parsons, P. A. Tasker and R. E. P. Winpenny, *J. Chem. Soc., Dalton Trans.*, 2000, 2349–2356.
39 Z. He, E.-Q. Gao, Z.-M. Wang, C.-H. Yan and M. Kurmoo, *Inorg. Chem.*, 2005, **44**, 862–874.
40 A. W. Addison, T. N. Rao, J. Reedijk, J. van Rijn and G. C. Verschoor, *J. Chem. Soc., Dalton Trans.*, 1984, 1349–1356.
41 H. Li, S.-G. Zhang, L.-M. Xie, L. Yu and J.-M. Shi, *J. Coord. Chem.*, 2011, **64**, 3595–3608.
42 S. Tsuzuki and A. Fujii, *Phys. Chem. Chem. Phys.*, 2008, **10**, 2584–2594.
43 P. Konieczny, A. B. Gonzalez-Guillén, K. Luberda-Durnaś, E. Čižmár, R. Pełka, M. Oszajca and W. Łasocha, *Dalton Trans.*, 2019, **48**, 7560–7570.
44 R. Boča, C. Rajnák, J. Titiš and D. Valigura, *Inorg. Chem.*, 2017, **56**, 1478–1482.
45 W. Jabeur, M. Korb, M. Hamdi, M. Holub, D. Princík, V. Zeleňák, A. Sanchez-Coronilla, M. Shalash, E. Čižmár and H. Naïli, *RSC Adv.*, 2024, **14**, 25048–25061.
46 R. Mičová, C. Rajnák, J. Titiš, E. Samoľová, M. Zalibera, A. Bieńko and R. Boča, *Chem. Commun.*, 2023, **59**, 2612–2615.
47 E. Pilichos, M. Font-Bardia, G. Aullón, J. Mayans and A. Escuer, *Inorg. Chem.*, 2024, **63**, 20415–20426.
48 S. Vitushkina, I. Potočňák, O. Bukrynov, L. Váhovská, M. Holub and E. Čižmár, *ChemistryOpen*, 2025, e202500109.
49 S. Ghosh, S. Kamilya, M. Das, S. Mehta, M.-E. Boulon, I. Nemec, M. Rouzieres, R. Herchel and A. Mondal, *Inorg. Chem.*, 2020, **59**, 7067–7081.
50 S. Chorazy, J. Wang and S. Ohkoshi, *Chem. Commun.*, 2016, **52**, 10795–10798.
51 A. Arauzo, A. Lazarescu, S. Shova, E. Bartolomé, R. Cases, J. Luzón, J. Bartolomé and C. Turta, *Dalton Trans.*, 2014, **43**, 12342–12356.
52 E. Pilichos, M. Font-Bardia, A. Escuer and J. Mayans, *Dalton Trans.*, 2022, **51**, 17653–17663.
53 E. Pilichos, P. Bhunia, M. Font-Bardia, A. Ghosh, J. Mayans and A. Escuer, *Dalton Trans.*, 2022, **51**, 1779–1783.
54 S. Xue, L. Ungur, Y.-N. Guo, J. Tang and L. F. Chibotaru, *Inorg. Chem.*, 2014, **53**, 12658–12663.
55 A. C. Benniston, S. Melnic, C. Turta, A. B. Arauzo, J. Bartolomé, E. Bartolomé, R. W. Harrington and M. R. Probert, *Dalton Trans.*, 2014, **43**, 13349–13357.
56 E. Bartolomé, J. Bartolomé, S. Melnic, D. Prodius, S. Shova, A. Arauzo, J. Luzón, L. Badía-Romano, F. Luis and C. Turta, *Dalton Trans.*, 2014, **43**, 10999–11013.
57 P. Bhunia, S. Dutta, S. Maity, J. Mayans, A. Escuer and A. Ghosh, *Inorg. Chim. Acta*, 2023, **545**, 121264.
58 A. Arauzo, E. Bartolomé, A. C. Benniston, S. Melnic, S. Shova, J. Luzón, P. J. Alonso, A.-L. Barra and J. Bartolomé, *Dalton Trans.*, 2017, **46**, 720–732.
59 S. Caballero, E. Pilichos, M. Font-Bardia, J. Mayans and A. Escuer, *Cryst. Growth Des.*, 2023, **23**, 3711–3719.
60 P.-E. Car, M. Perfetti, M. Mannini, A. Favre, A. Caneschi and R. Sessoli, *Chem. Commun.*, 2011, **47**, 3751–3753.
61 A. C. Benniston, S. Melnic, C. Turta, A. B. Arauzo, J. Bartolomé, E. Bartolomé, R. W. Harrington and M. R. Probert, *Dalton Trans.*, 2014, **43**, 13349–13357.
62 K. Hchicha, M. Korb, A. Kliuikov, E. Čižmár and H. Naïli, *J. Magn. Magn. Mater.*, 2021, **536**, 168140.
63 L. Tesi, A. Lunghi, M. Atzori, E. Lucaccini, L. Sorace, F. Totti and R. Sessoli, *Dalton Trans.*, 2016, **45**, 16635–16643.
64 D. Aravena and E. Ruiz, *Dalton Trans.*, 2020, **49**, 9916–9928.
65 Bruker, *Apex 5*; Bruker AXS Inc.: Madison, Wisconsin, USA, 2023.
66 G. A. Bain and J. F. Berry, *J. Chem. Educ.*, 2008, **85**, 532.
67 S. Stoll and A. Schweiger, *J. Magn. Reson.*, 2006, **178**, 42–55.
68 A. L. Pellegrino, C. Mezzalira, F. Mazzer, L. C. Tazi, A. Caneschi, D. Gatteschi, I. L. Fragalà, A. Speghini, L. Sorace and G. Malandrino, *Inorg. Chim. Acta*, 2022, **535**, 120851.
69 CCDC 2264081: Experimental Crystal Structure Determination, 2026, DOI: 10.5517/ccdc.csd.cc2fzyw8.